ACS Energy LETTERS

http://pubs.acs.org/journal/aelccp

Improved Phase Stability of Formamidinium Lead Triiodide Perovskite by Strain Relaxation

Xiaojia Zheng,*[†] Congcong Wu,[†] Shikhar K. Jha,[†] Zhen Li,[‡] Kai Zhu,*[‡] and Shashank Priya*[†]

[†]Center for Energy Harvesting Materials and System, Virginia Tech, Blacksburg, Virginia 24061, United States
[‡]Chemistry and Nanoscience Center, National Renewable Energy Laboratory, Golden, Colorado 80401, United States

Supporting Information

ABSTRACT: Though formamidinium lead triiodide ($FAPbI_3$) possesses a suitable band gap and good thermal stability, the phase transition from the pure black perovskite phase (α-phase) to the undesirable yellow nonperovskite polymorph (δ-phase) at room temperature, especially under humid air, hinders its practical application. Here, we investigate the intrinsic instability mechanism of the α-phase at ambient temperature and demonstrate the existence of an anisotropic strained lattice in the (111) plane that drives phase transformation into the δ-phase. Methylammonium bromide (MABr) alloying (or $FAPbI_3$-MABr) was found to cause lattice contraction, thereby balancing the lattice strain. This led to dramatic improvement in the stability of α-$FAPbI_3$. Solar cells fabricated using $FAPbI_3$-MABr demonstrated significantly enhanced stability under the humid air.

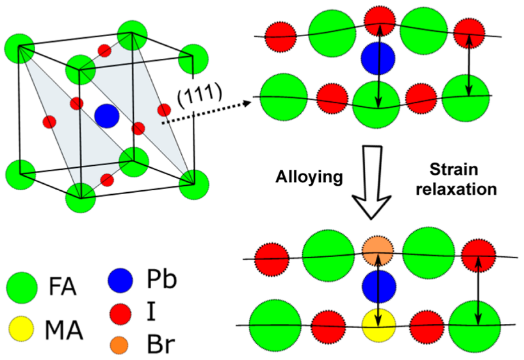

Methylammonium (MA) lead halide perovskite films ($CH_3NH_3PbX_3$, where CH_3NH_3 = MA, X = I, Br, or Cl) are promising materials to be used as active layers in photovoltaic (PV) and light-emitting devices owing to their high light absorption coefficient, long charge carrier diffusion lengths, ambipolar charge transport, and solution processability.[1−3] However, their stability under light, moisture, and/or heat is a potential issue hindering their commercialization. The intrinsic thermal instability of $MAPbI_3$ is one of the important stability issues, caused by its low formation energy, low thermal conductivity, and the phase transition near ~57 °C. The calculated formation energy per unit cell (0.11−0.14 eV) for $MAPbI_3$ perovskite is quite close to the average thermal energy at 85 °C (0.093 eV),[4] a condition that can be easily reached due to heat accumulation when the cell is operating under direct sunlight. The low thermal conductivity (~0.5 W/[K m] at room temperature) restricts heat dissipation in the perovskite layer, resulting in increased thermal mass.[5] Another issue arises due to the low phase transition temperature of 57 °C (tetragonal to cubic) that can cause a big volume change in the perovskite layer,[6] resulting in buildup of mechanical stress that limits the lifetime of the perovskite solar cells (PSCs). Though $CH_3NH_3PbX_3$ single crystals and thin films prepared by vacuum-based methods present better thermal stability,[7−9] the environmental stability is still an open challenge. Thus, heat-tolerant perovskite absorbers are necessary for long-term thermal stability of PSCs.

The exchange of organic cations in perovskites from MA to formamidinium (FA) results in a material with a smaller band gap and higher thermal stability, which could lead to better and more reliable performance.[10−13] Snaith et al. characterized the thermal stability of $FAPbI_3$ and $MAPbI_3$ in air up to 150 °C. The former showed higher stability without bleaching even after 60 min, while the latter was bleached within 30 min.[10] Despite the good thermal stability of $FAPbI_3$, it is challenging to obtain and maintain its pure black perovskite phase (α-phase, pseudocubic) at room temperature due to the phase transition from the α-perovskite polymorph to the undesirable yellow nonperovskite polymorph (δ-phase, hexagonal), especially under humid air.[13−17] Better stability was observed for both Cs- and MA- alloyed $FAPbI_3$, which was due to enhanced interaction between the FA ion and iodine or a decrease in the tolerance factor.[14,16,18,19] These studies suggest that alloying might be a feasible pathway toward improving the inherent phase stability of $FAPbI_3$ perovskite material. However, in-depth understanding of the operating mechanism behind this increased stability has not been achieved, which is preventing further progress.

X-ray diffraction (XRD) is a powerful tool for characterizing the crystallographic structure, chemical composition, and physical properties of materials. From XRD analysis, we find that α-$FAPbI_3$ has an anisotropic strained lattice (higher strain in the (111) plane). In contrast, δ-$FAPbI_3$ is almost strain free. We hypothesize that strain in the (111) plane of the α-phase is a driving force for its easy phase transition into the δ-phase, where the (111) plane acts as the nucleation site for the (0001)

Received: September 19, 2016
Accepted: October 18, 2016
Published: October 18, 2016

ACS Publications

DOI: 10.1021/acsenergylett.6b00457
ACS Energy Lett. 2016, 1, 1014−1020

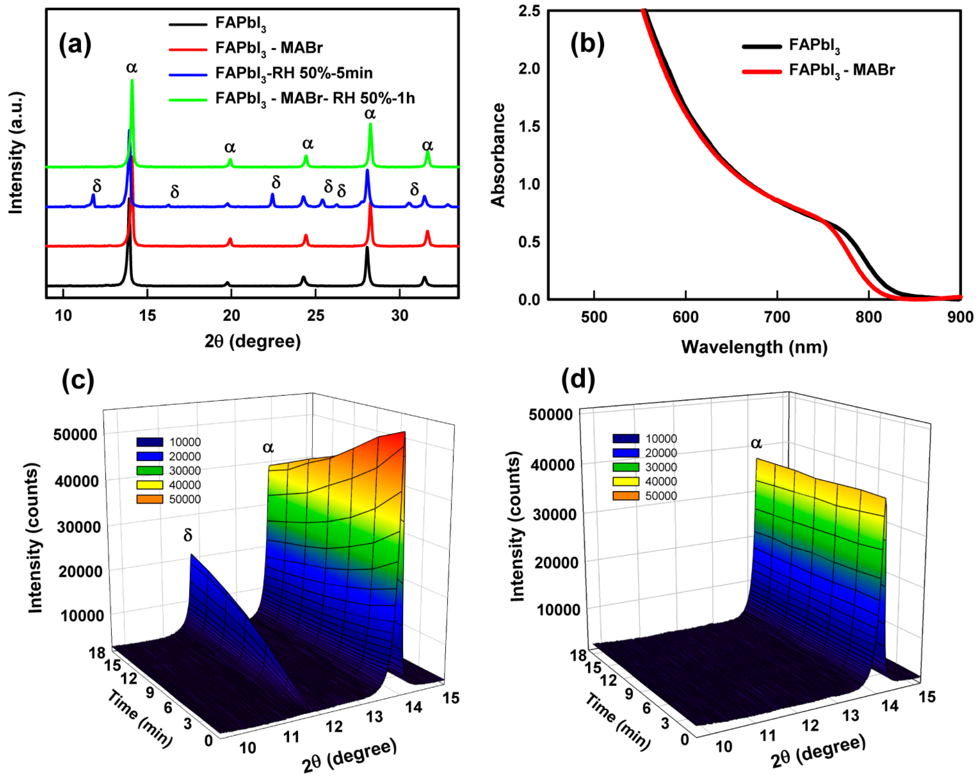

Figure 1. (a) XRD patterns of FAPbI$_3$ and FAPbI$_3$-MABr thin films before and after exposure to humid air. (b) UV−vis absorption spectra of the as-deposited FAPbI$_3$ and FAPbI$_3$-MABr thin films. Time-dependent XRD measurements of (c) FAPbI$_3$ with phase transition and (d) stabilized FAPbI$_3$-MABr without phase transition under a humid atmosphere with a RH of ∼50% at 23 °C.

plane of the δ-phase. When FAPbI$_3$ is alloyed with MABr (alloyed FAPbI$_3$ is denoted as FAPbI$_3$-MABr), the lattice size is reduced and strain in the grain is relaxed; thus, the pseudocubic α-phase is stabilized at room temperature, even under humid air. The solar cells fabricated by using FAPbI$_3$-MABr perovskite layer show an efficiency of ∼16% for a small area (0.096 cm^2), and ∼15% for a large area (0.48 cm^2) with fast photoresponse and negligible J−V hysteresis. More importantly, the MABr-alloyed PSC can maintain its efficiency without any degradation in all device parameters for more than 1000 h under a high relative humidity (RH) of ∼50% at 23 °C. In contrast, the solar cells fabricated by using pristine FAPbI$_3$ can only maintain ∼10% of the initial value after 2 h under similar conditions. These findings clearly address the complex problem of stabilizing the α-FAPbI$_3$ in an ambient atmosphere, which can be realized through a simple device fabrication process.

It is well-known that MAPbI$_3$ is very sensitive to humid air as its color normally changes from dark brown to yellow in less than 24 h due to the material decomposition from MAPbI$_3$ to PbI$_2$ under high humidity.[20] We found that when FAPbI$_3$ films were kept in air with a RH of ∼50% at 23 °C, the color of the film also changed from dark brown to yellowish within several minutes, which is much faster than MAPbI$_3$ (Figure S1). However, from the XRD results shown in Figure 1a, we cannot find any diffraction peaks related to PbI$_2$; rather, new peaks are attributable to the nonperovskite polymorph (δ-phase) of FAPbI$_3$.[14,19] Though the color of both MAPbI$_3$ and FAPbI$_3$ can change from dark brown to yellow, unlike the MAPbI$_3$, the color change of FAPbI$_3$ results from phase transition, rather than chemical degradation. It has been reported that δ-FAPbI$_3$ is more stable than α-FAPbI$_3$ at room temperature, and α-FAPbI$_3$ will change to δ-FAPbI$_3$ even under dry air with aging.[14] We also notice that the color transformation was much slower if the dark brown FAPbI$_3$ films were kept in dry air (it takes several weeks before an obvious color change). Thus, our results indicate that the humid air can accelerate this phase transition process to a great extent. Interestingly, when part of FAI is changed to MABr, the resulting FAPbI$_3$-MABr material shows excellent stability under an ambient environment. As shown in Figure 1a, the XRD peaks of α-FAPbI$_3$ shift to higher angles for FAPbI$_3$-MABr due to a more compact lattice, along with the blue shift (∼15 nm) of the absorption onset after the alloying process (Figure 1b), indicating successful incorporation of MABr in FAPbI$_3$. For FAPbI$_3$-MABr, there is no change in their color (Figure S2) and XRD pattern (Figure 1a) even after 1 h under the same humid conditions (RH ≈ 50%, 23 °C). Figure 1c,d shows time-dependent XRD measurements of unstable pure FAPbI$_3$ with a phase transition and stabilized FAPbI$_3$-MABr without a phase transition under the same humid atmosphere. The reflection peaks around 11.8° and 13.9° in Figure 1c are linked to the reflections of δ-FAPbI$_3$ and α-FAPbI$_3$ phases, respectively. We can see that the peak at 11.8° starts to emerge immediately after exposure of the pure FAPbI$_3$ to humid air, indicating initiation of phase transition. As the peak at 11.8° becomes stronger, the peak intensity at 13.9° becomes weaker with time, caused by the continuous phase transition. No peak related to PbI$_2$ appears during the whole process (the peak for PbI$_2$ is located at 12.7°). In contrast, FAPbI$_3$-MABr exhibits no phase transition under the same conditions (Figure 1d). On the basis of the results shown here, we conclude that the moisture in air can accelerate the phase transition from α-FAPbI$_3$ to δ-FAPbI$_3$ at room temperature, and the MABr can stabilize the α-FAPbI$_3$ under humid air, thus

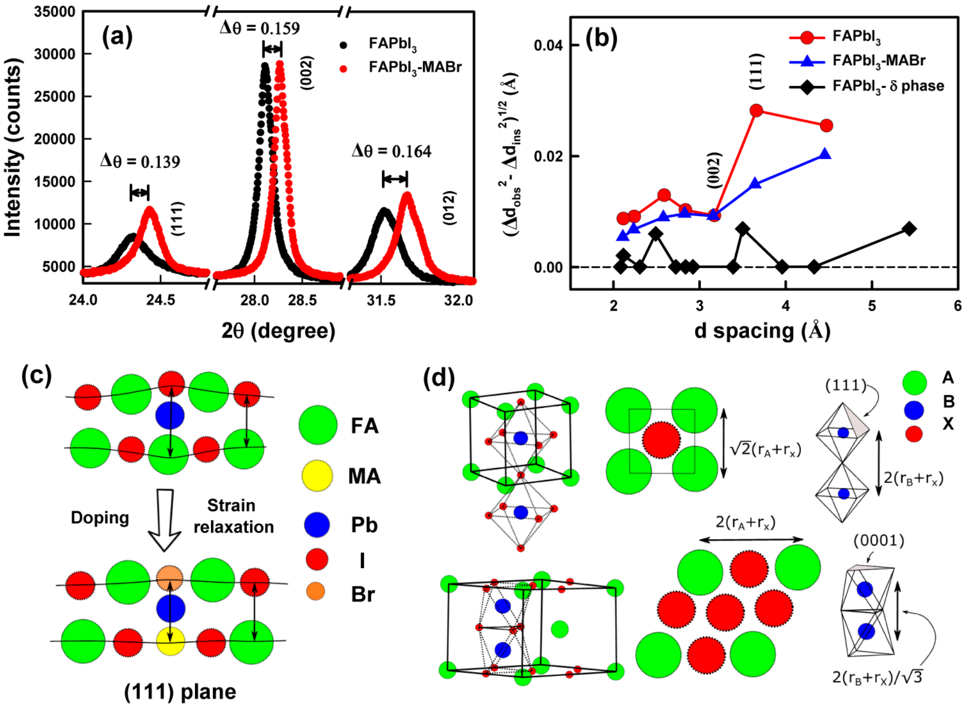

Figure 2. (a) Magnification of XRD results comparing the peak shift after MABr alloying. (b) Williamson−Hall plot of $(\Delta d_{obs}^2 - \Delta d_{ins}^2)^{1/2}$ versus interplanar spacing of different planes, extracted from the corresponding diffraction profiles shown in Figure S3. (c) Schematic representation of strain relaxation after MABr alloying (side view) and (d) the structure and corresponding lattice parameters of the pseudocubic α-phase and hexagonal δ-phase.

providing a material with higher tolerance to environmental constraints.

There is a strong relationship between the property/function and structure of the material; therefore, we next try to identify the mechanism behind improved stability by comparing the crystal structures before and after alloying. We hypothesize that phase transformation from the α- to δ-phase in FAPbI$_3$ is the guiding factor. On the basis of our results, we found that MABr alloying has two effects on structure: reducing the lattice volume and relaxing the strain in lattice. From the XRD pattern shown in Figure 2a, peaks shift toward higher angles after MABr alloying, indicating shrinkage of the lattice according to the Braggs law, $n\lambda = 2d_{hkl}\sin\theta$. When the peak location is converted into a lattice constant, using eq 1, we can deduce an isotropic reduction in the size of the unit cell (Table S1).

$$a = \frac{d_{hkl}}{\sqrt{h^2 + k^2 + l^2}} \tag{1}$$

where a is the lattice constant, d_{hkl} is the interplanar spacing of the (hkl) plane, and h, k, and l are the Miller indices. In addition to a shift in the peak position, we also notice the sharpening of some peaks in Figure 2a that are related to strain relaxation of the lattice. When strain is introduced in a material, the lattice planes distort to accommodate these structural defects. This leads to a different interplanar distance across the material, reflected by broadening of the diffraction peaks.[21−23] In principle, the observed peak broadening in every (hkl) plane is a convolution of instrumental broadening, nanoscale grain sizes, and strain (or microstrain in this case) in the lattice, as mathematically expressed by eq 2[22]

$$\Delta d_{obs}^2 = \Delta d_{inst}^2 + \Delta d_{size}^2 + \Delta d_{\varepsilon}^2 \tag{2}$$

where, Δd_{obs} is the difference in d-spacing at full width at half-maximum (fwhm) for a given (hkl) plane; Δd_{inst}, Δd_{size}, and Δd_{ε} are the contributions of the instrument, grain size, and strain related to the observed peak width, respectively. The Δd_{size} is small and can be neglected due to the large grain sizes for both materials (several hundred nanometers, Figure S4). Therefore, eq 2 gives us a linear relation in terms of strain as

$$\Delta d_{\varepsilon} = \sqrt{\Delta d_{obs}^2 - \Delta d_{inst}^2} = \varepsilon \cdot d \tag{3}$$

where ε is the unitless strain in the lattice (given by $\Delta d_{\varepsilon}/d$) and d is the interplanar spacing for different (hkl) planes. Here Δd_{inst} can be obtained by running an XRD pattern on a calibration standard (LaB$_6$ specimen) under the same settings. A linear fitting is obtained that is then subtracted from observed values (Figure S5). The relation between peak broadening and d-spacing is plotted in Figure 2b for all FAPbI$_3$, MABr-FAPbI$_3$, and δ-FAPbI$_3$. The plot gives us an unusual finding; while FAPbI$_3$-MABr has an almost linear fitting, α-FAPbI$_3$ shows an erratic pattern. The slope of this linear fitting between peak broadening and interplanar distance suggests that strain in the structure is uniformly distributed in FAPbI$_3$-MABr. However, in the case of pure FAPbI$_3$, the erratic pattern with larger value means a higher and anisotropic strain. The higher broadening of the (111) peak and sharper (002) peak means that there is higher strain in the (111) plane and lower strain in the (002) plane (confirmed with three different samples of FAPbI$_3$, Figure S6). This high strain in the (111) plane is developed because of deviation from the equilibrium interplanar distances, while the MABr alloying can relax the strain in (111), as can be understood by Figure 2c. Pure α-FAPbI$_3$ (ABX$_3$) has a perovskite structure with six-fold PbI$_6$ octahedra occupying the middle of the pseudocubic structure and connected to another octahedra by corner sharing (Figure 2d). The FA

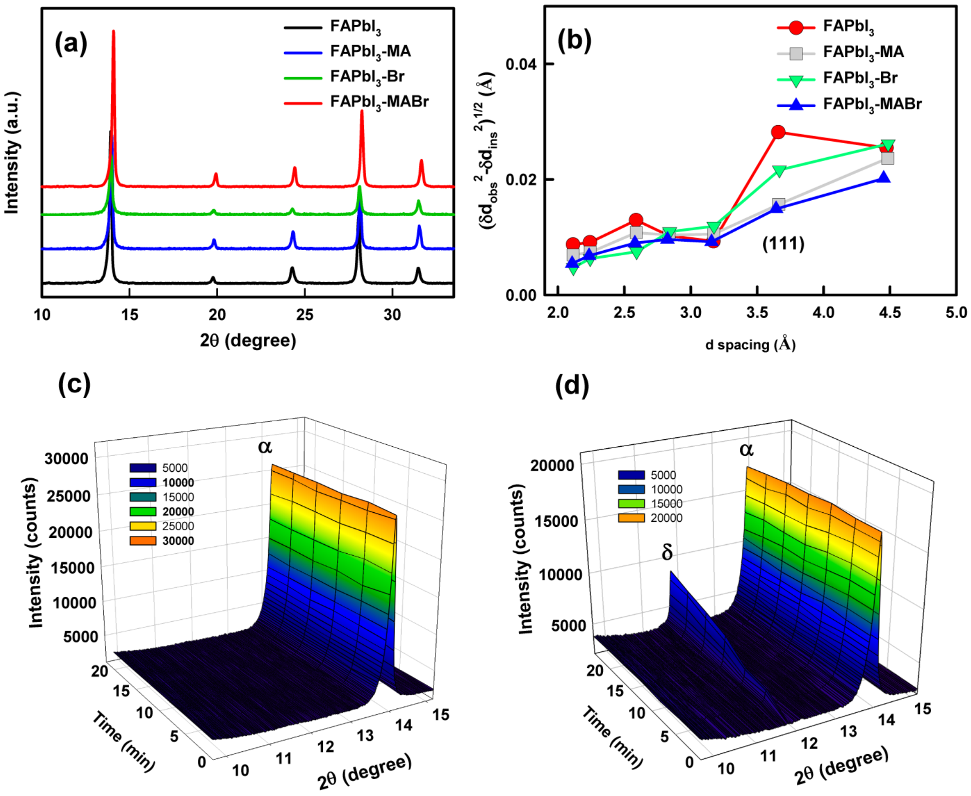

Figure 3. (a) XRD patterns of the as-synthesized $FAPbI_3$ and $FAPbI_3$-MA, $FAPbI_3$-Br, and $FAPbI_3$-MABr thin films. (b) Williamson−Hall plot of $(\Delta d_{obs}^2 - \Delta d_{ins}^2)^{1/2}$ versus interplanar spacing of different planes, extracted from the corresponding diffraction profiles shown in (a). Phase transition test of (c) $FAPbI_3$-MA and (d) $FAPbI_3$-Br under a humid atmosphere with a RH of ∼50% at 23 °C.

molecule (A-sites), which is considerably larger than Pb (B-sites) (FA^+ = 253 pm, Pb^{2+} = 120 pm, I^- = 220 pm),[24] sits in 12-fold coordination. A slight variation from ideal size of atoms/molecules is usually accommodated by rotation/tilt in the octahedral arrangement, but when the A-sites become too big to accommodate (as is the case here), it transforms into a more stable hexagonal structure (δ phase), with PbI_6 octahedra sharing faces rather than corners. This brings Pb−Pb closer and separates the distance between FA and FA. A quick calculation on the closest distance between FA−FA and Pb−Pb distances is shown in Figure 2d. For the hexagonal structure, a shorter distance for FA−FA is $\sqrt{2}$ times bigger than that for the α-phase. Separation between bigger atoms at the expense of smaller atoms getting closer (Pb−Pb) is the reason for the higher stability of hexagonal phase as the total energy of the system through this arrangement is lowered. A similar observation was made while investigating the phase transition of another perovskite $SrMnO_3$.[25] As the hexagonal structure has the same atomic arrangement in the (0001) plane as that of (111) of the cubic lattice (both being closed-packing planes of FA and Pb), the strain in (111) planes helps to nucleate (0001) of the hexagonal phase with less activation energy. We do find evidence that after the transformation the strain in δ-$FAPbI_3$ is almost nonexistent (Figure 2b). Thus, we arrive at the conclusion that MABr alloying can relax the strain in the (111) plane and thereby prevent the phase transition from the α-phase to δ-phase.

Note that both MA and Br can lead to reduction of the lattice strain, thereby stabilizing the α-phase of the perovskite. To address the different roles of MA and Br with respect to the stability of $FAPbI_3$, both MA-alloyed perovskite (denoted by $FAPbI_3$-MA) and Br-alloyed perovskite (denoted by $FAPbI_3$-Br) were also fabricated to compare with $FAPbI_3$-MABr; the respective amounts of MA and Br were controlled at the same level as that in $FAPbI_3$-MABr. Peaks shift to a higher angle for all alloying materials (Figure 3a), which indicates the successful substitution of ions in the $FAPbI_3$ lattice. Figure 3b provides the relationship between the Williamson−Hall plot and d-spacing for all four samples shown in Figure 3a. $FAPbI_3$-MA shows a linear plot similar to that for $FAPbI_3$-MABr. However, $FAPbI_3$-Br is more like $FAPbI_3$, displaying an irregular pattern but with a smaller strain in the (111) plane. Thus, MA, Br, or MABr alloying can relax the strain in the (111) plane and induce functional change. According to Kieslich's work,[24] the effective radii difference between FA^+ and MA^+ is 36 pm, larger than the difference between I^- and Br^- (24 pm); therefore, the substitution with MA^+ plays a more effective role in changing the lattice structure than Br^-. Note that compared with MA^+ (15% on A site), the percentage of Br is much lower (5% in halide), which may be another reason for insufficient capacity to balance the anisotropic strain in the (111) plane. Figure 3c,d provides the stability test result for $FAPbI_3$-MA and $FAPbI_3$-Br under a humid atmosphere. No phase transition was observed for $FAPbI_3$-MA, indicating a stable phase structure under humid air due to the reduced strain in the (111) plane. For $FAPbI_3$-Br, the peak located at 11.8°, representing the reflections of δ-$FAPbI_3$, becomes stronger with time, while, unlike the $FAPbI_3$, the peak intensity of the α-phase does not change. The phase was stabilized to some extent but not as efficiently as $FAPbI_3$-MA or $FAPbI_3$-MABr. On the basis of these results, we conclude that both MA and Br show the ability

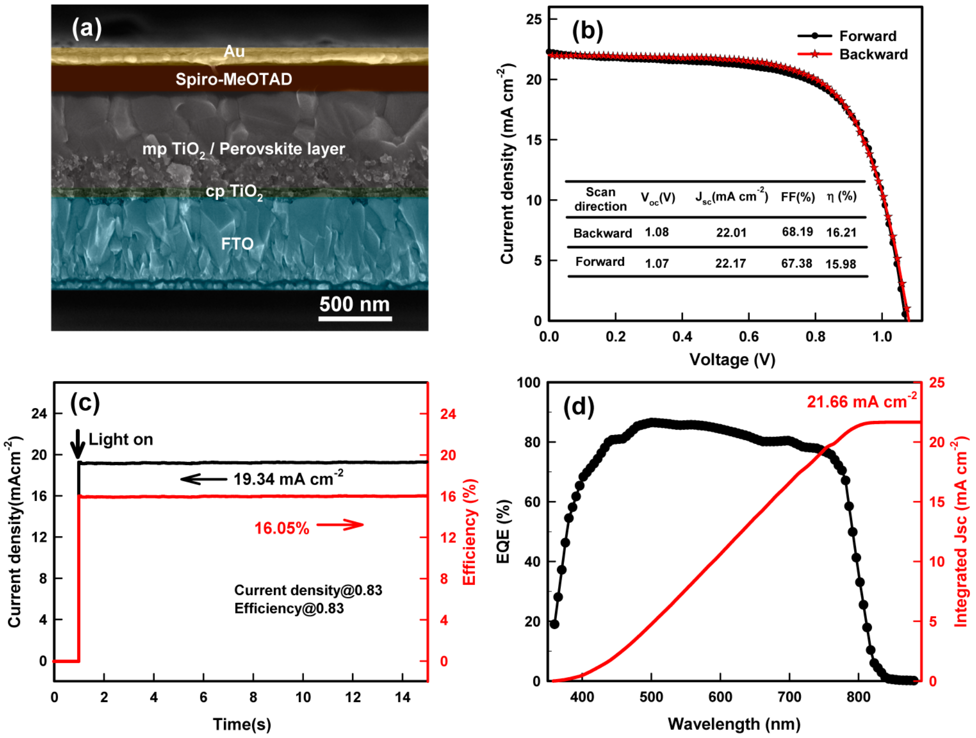

Figure 4. (a) Cross-sectional SEM image of the FAPbI$_3$-MABr PSCs. (b) Typical J−V curves and extracted PV parameters, (c) the corresponding stabilized output of the PCE and J at the maximum power point as a function of time for the solar cell under simulated 1 sun illumination, and (d) EQE spectra. The active area of the solar cell is 0.096 cm^2.

to stabilize the perovskite phase of FAPbI$_3$ and MA plays the dominant role in improving the stability.

Considering all of the evidence that we have presented above, it appears that the MABr alloying results in stable α-FAPbI$_3$ even under humid air. To further investigate their stability in a solar cell, we fabricated PV devices with both FAPbI$_3$ and FAPbI$_3$-MABr. Figure 4a shows the microstructure of the FAPbI$_3$-MABr device. A 60 nm thick compact TiO$_2$ layer, prepared by he sol−gel method, was used as the hole-blocking layer, and then, a 200 nm mesoporous TiO$_2$ layer was deposited onto it by spin coating, which enhances the charge separation and collection, thereby relieving the hysteresis effect of PSCs under different scan directions during the measurements.[26] A continuous, flat, and dense perovskite film with a thickness of ∼450 nm fully covered the top surface of the mesoporous TiO$_2$ layer, along with partial infiltration into the mesoporous TiO$_2$ layer. On top of the perovskite layer, a 200 nm thick spiro-OMeTAD was deposited, which acts as the hole transport material (HTM). Figure 4b presents current density−voltage (J−V) curves measured with a 120 ms scanning delay for each measured data point in backward (from the open-circuit voltage (V_{oc}) to the short-circuit current (J_{sc})) and forward (from J_{sc} to V_{oc}) modes under standard AM 1.5G (air mass 1.5 global) illumination of the FAPbI$_3$-MABr device. From the corresponding PV performance, we derive values of 22.01 mA cm^2, 1.08 V, and 68.19% for J_{sc}, V_{oc}, and the fill factor (FF), respectively, yielding a PCE of 16.21% for the backward scan. For the forward scan, the device shows a J_{sc} of 22.17 mA cm^2, a V_{oc} of 1.07 V, a FF of 67.38%, and a PCE of 15.98%. During the measurement, the change in the bias voltage requires a charge redistribution to reach a new equilibrium state, and the generated charge carriers require significant time for charge distribution in hybrid PSCs.[27] Therefore, rapid scanning of the applied voltage often leads to a huge hysteresis in the J−V results. In our case, the hysteresis effect is negligible, benefiting from the mp-TiO$_2$ layer, which can enhance charge collection from the perovskite layer via a large TiO$_2$ interface. The performance of solar cells based on FAPbI$_3$ as the light absorber is shown in Figure S8, and the corresponding PV parameters are summarized in Table S2. Though its absorption is broader than that of FAPbI$_3$-MABr, J_{sc} is much lower (17 mA cm^2). Before depositing the gold layer (the cleanroom has the RH value fixed at 43%), we had to transfer our samples from the glovebox to the e-beam chamber. Exposure of the thin films to humid air during the transfer process may introduce a phase transition (as the phase transition process can be accelerated by moist air). That may be the reason for the lower J_{sc} than the predicted value. The J−V hysteresis effect is also higher than that of the FAPbI$_3$-MABr solar cell, probably due to the impure phase. Figure 4c shows the steady output power test for the FAPbI$_3$-MABr solar cell. We set the external bias at 0.83 V, and the output current density was monitored with time. The current density increased sharply when we turned on the light and stabilized at 19.34 mA cm^2, yielding a PCE of ∼16.05%. On the basis of our previous results, faster dynamic current response always shows lower hysteresis in the device, which agrees with the J−V results shown in Figure 4b.[28] The external quantum efficiency (EQE) for the FAPbI$_3$-MABr solar cell is shown in Figure 4d, with a broad plateau above 70% in the wavelength range of 400−780 nm. A high EQE suggests that solar light can be efficiently converted to charge carriers and collected by the terminal electrode, which is responsible for the larger photocurrent density of the solar cell. We notice the cutoff of the EQE is around 820 nm, which makes a small blue shift compared with the well-known FAPbI$_3$ material (840 nm) due to the larger band gap after the cation and anion

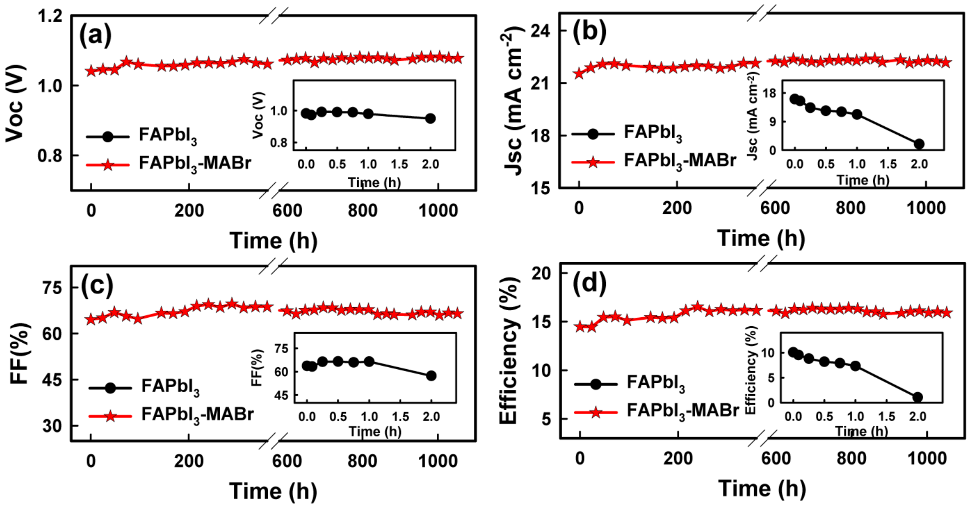

Figure 5. Comparative analysis of the performance parameters: (a) V_{oc}, (b) J_{sc}, (c) FF, and (d) PCE of solar cells based on FAPbI$_3$ (insets) and FAPbI$_3$-MABr with time stored in air under a RH of ∼50% at 23 °C without encapsulation.

substitution, as noticed in the absorption spectra in Figure 1b.[10,17] Twenty independent solar cells were fabricated on the same substrate with a size of 1 in. × 1 in. to investigate the uniformity of the perovskite layer. The spatial distributions of their performance are shown in Figure S9. Most devices have efficiencies of ∼16%, except for the ones located on the four corners. This result shows that the uniformity of the thin films is excellent. Solar cells with an area of 0.48 cm^2 in an oblong shape were also fabricated. $J-V$ curves, the corresponding PV parameters, and the stabilized output of PCE and J at the maximum power point under simulated 1 sun illumination are shown in Figure S10. Similar to the solar cells with an active area of 0.096 cm^2, the hysteresis effect is negligible with a PCE of ∼15%.

Finally, we investigated the device stability of both FAPbI$_3$-MABr solar cells (Figure 5) and FAPbI$_3$ (insets), kept under humid air (RH ≈ 50%, 23 °C). The performance of the pure FAPbI$_3$ solar cell degraded rapidly. Only 10% of the initial value remained after only 2 h, and the color of the solar cell changed from dark brown to yellowish. The main decrease of the performance was contributed from the decrease of J_{sc} due to the film transformation from the black phase to the yellow phase. We noticed that the color change of the device was much slower than that of the bare thin film shown in Figure S1. It took about 0.5 h for the spiro-OMeTAD-covered region and 1 h for the Au-covered region to change to a yellowish color, while for the thin film directly exposed to moist air with the same RH, the color changed to yellowish in about 10 min. The spiro-OMeTAD and Au layer served as a protection barrier and kept the performance of the pure FAPbI$_3$ device with a J_{sc} >10 mA cm^2 even after 1 h. We further kept the same solar cell in a glass desiccator with RH ≈ 50% and found that the solar cell could maintain an efficiency of 0.35% with a J_{sc} of 1.12 mA cm^2 even after 1 week (Table S3). To our surprise, the V_{oc} was 0.92 V, not far below the pristine value of 0.98 V (Figure S11), which indicated that the yellow phase also showed obvious PV effect. On the other hand, the FAPbI$_3$-MABr solar cell showed high stability under humid air. No drop in the efficiency was observed for the solar cell kept under a RH of ∼50% for 1000 h. A slight increase of the performance at the first stage may be attributed to the oxidation of spiro-OMeTAD.[29] Though the PV performance can be retained after such a long time, we noticed that the color of the perovskite film, which was not covered by Au, changes to a bit lighter shade, indicating that encapsulation may be needed for practical applications.

In summary, we have investigated the phase transition of FAPbI$_3$ in ambient air. The results show that the existing anisotropic strained lattice in the (111) plane in FAPbI$_3$ can help the α-phase transform into the δ-phase, and humid air can accelerate this process. MABr alloying can provide a more compact crystal lattice (thus increasing Coulomb interactions within the structure) and relax strain in the lattice, thereby stabilizing the α-phase of FAPbI$_3$. Solar cells using FAPbI$_3$ as the light absorber show an obvious hysteresis effect and low stability under humid air due to the phase transition problems. Air-stable solar cells with good performance (∼16% for 0.096 cm^2; ∼15% for 0.48 cm^2) and low hysteresis are obtained based on the lattice strain balanced material (FAPbI$_3$-MABr). On the basis of these observations, we propose that releasing the strain in FAPbI$_3$ by alloying can stabilize the perovskite structure of FAPbI$_3$ and reduce the sensitivity to humid air against α-to-δ phase transformation, which will potentially give a stable perovskite device and simplify the fabrication process significantly.

■ ASSOCIATED CONTENT

Ⓢ Supporting Information

The Supporting Information is available free of charge on the ACS Publications website at DOI: 10.1021/acsenergylett.6b00457.

> Experimental section, Figures S1−S11, showing the surfaces under different conditions, XRD patterns and fitting results, SEM images, and $J-V$ curves, and Tables S1−S3, showing calculated lattices constants and photovoltaic parameters (PDF)

■ AUTHOR INFORMATION

Corresponding Authors

*E-mail: xiaojia@vt.edu (X.Z.).
*E-mail: kai.zhu@nrel.gov (K.Z.).
*E-mail: spriya@vt (S.P.).

Notes

The authors declare no competing financial interest.

■ ACKNOWLEDGMENTS

The authors acknowledge financial support from the Institute of Critical Technology and Applied Science (ICTAS). S.P. and X.Z. would also like to acknowledge financial support from the Office of Naval Research through the MURI program. S.K.J. was supported through the Office of Naval Research participation in NSF I/UCRC: Center for Energy Harvesting Materials and Systems (CEHMS). The work at the National Renewable Energy Laboratory is supported by the U.S. Department of Energy under Contract No. DE-AC36-08-GO28308. K.Z. and Z.L. acknowledge support by the hybrid perovskite solar cell program of the National Center for Photovoltaics funded by the U.S. Department of Energy, Office of Energy Efficiency and Renewable Energy, Solar Energy Technologies Office.

■ REFERENCES

(1) Fang, Y.; Huang, J. Resolving weak light of sub-picowatt per square centimeter by hybrid perovskite photodetectors enabled by noise reduction. *Adv. Mater.* **2015**, *27*, 2804−2810.

(2) Shi, D.; Adinolfi, V.; Comin, R.; Yuan, M.; Alarousu, E.; Buin, A.; Chen, Y.; Hoogland, S.; Rothenberger, A.; Katsiev, K.; et al. Low trap-state density and long carrier diffusion in organolead trihalide perovskite single crystals. *Science* **2015**, *347*, 519−522.

(3) Zheng, X.; Chen, B.; Yang, M.; Wu, C.; Orler, B.; Moore, R. B.; Zhu, K.; Priya, S. The controlling mechanism for potential loss in $CH_3NH_3PbBr_3$ hybrid solar cells. *ACS Energy Lett.* **2016**, *1*, 424−430.

(4) Conings, B.; Drijkoningen, J.; Gauquelin, N.; Babayigit, A.; D'Haen, J.; D'Olieslaeger, L.; Ethirajan, A.; Verbeeck, J.; Manca, J.; Mosconi, E.; et al. Intrinsic thermal instability of methylammonium lead trihalide perovskite. *Adv. Energy Mater.* **2015**, *5*, 1500477.

(5) Pisoni, A.; Jaćimović, J.; Barišić, O. S.; Spina, M.; Gaál, R.; Forró, L.; Horváth, E. Ultra-low thermal conductivity in organic−inorganic hybrid perovskite $CH_3NH_3PbI_3$. *J. Phys. Chem. Lett.* **2014**, *5*, 2488−2492.

(6) Baikie, T.; Fang, Y.; Kadro, J. M.; Schreyer, M.; Wei, F.; Mhaisalkar, S. G.; Grätzel, M.; White, T. J. Synthesis and crystal chemistry of the hybrid perovskite $(CH_3NH_3)PbI_3$ for solid-state sensitised solar cell applications. *J. Mater. Chem. A* **2013**, *1*, 5628−5641.

(7) Liu, Y.; Yang, Z.; Cui, D.; Ren, X.; Sun, J.; Liu, X.; Zhang, J.; Wei, Q.; Fan, H.; Yu, F.; et al. Two-inch-sized perovskite $CH_3NH_3PbX_3$ (X = Cl, Br, I) crystals: Growth and characterization. *Adv. Mater.* **2015**, *27*, 5176−5183.

(8) Ku, Z.; Tiep, N. H.; Wu, B.; Sum, T. C.; Fichou, D.; Fan, H. J. Solvent engineering for fast growth of centimetric high-quality $CH_3NH_3PbI_3$ perovskite single crystals. *New J. Chem.* **2016**, *40*, 7261−7264.

(9) Zhang, J.; Zhao, Y.; Yang, D.; Li, C.; Liu, S. Highly stabilized perovskite solar cell prepared using vacuum deposition. *RSC Adv.* **2016**, *6*, 93525−93531.

(10) Eperon, G. E.; Stranks, S. D.; Menelaou, C.; Johnston, M. B.; Herz, L. M.; Snaith, H. J. Formamidinium lead trihalide: A broadly tunable perovskite for efficient planar heterojunction solar cells. *Energy Environ. Sci.* **2014**, *7*, 982−988.

(11) Pang, S.; Hu, H.; Zhang, J.; Lv, S.; Yu, Y.; Wei, F.; Qin, T.; Xu, H.; Liu, Z.; Cui, G. $NH_2CH{=}NH_2PbI_3$: An alternative organolead iodide perovskite sensitizer for mesoscopic solar cells. *Chem. Mater.* **2014**, *26*, 1485−1491.

(12) Amat, A.; Mosconi, E.; Ronca, E.; Quarti, C.; Umari, P.; Nazeeruddin, M. K.; Grätzel, M.; De Angelis, F. Cation-induced band-gap tuning in organohalide perovskites: Interplay of spin−orbit coupling and octahedra tilting. *Nano Lett.* **2014**, *14*, 3608−3616.

(13) Zhumekenov, A. A.; Saidaminov, M. I.; Haque, M. A.; Alarousu, E.; Sarmah, S. P.; Murali, B.; Dursun, I.; Miao, X.-H.; Abdelhady, A. L.; Wu, T.; et al. Formamidinium lead halide perovskite crystals with unprecedented long carrier dynamics and diffusion length. *ACS Energy Lett.* **2016**, *1*, 32−37.

(14) Li, Z.; Yang, M.; Park, J.-S.; Wei, S.-H.; Berry, J. J.; Zhu, K. Stabilizing perovskite structures by tuning tolerance factor: Formation of formamidinium and cesium lead iodide solid-state alloys. *Chem. Mater.* **2016**, *28*, 284−292.

(15) Weller, M. T.; Weber, O. J.; Frost, J. M.; Walsh, A. Cubic perovskite structure of black formamidinium lead iodide, α-$[HC(NH_2)_2]PbI_3$, at 298 k. *J. Phys. Chem. Lett.* **2015**, *6*, 3209−3212.

(16) Jeon, N. J.; Noh, J. H.; Yang, W. S.; Kim, Y. C.; Ryu, S.; Seo, J.; Seok, S. I. Compositional engineering of perovskite materials for high-performance solar cells. *Nature* **2015**, *517*, 476−480.

(17) Yang, W. S.; Noh, J. H.; Jeon, N. J.; Kim, Y. C.; Ryu, S.; Seo, J.; Seok, S. I. High-performance photovoltaic perovskite layers fabricated through intramolecular exchange. *Science* **2015**, *348*, 1234−1237.

(18) Lee, J.-W.; Kim, D.-H.; Kim, H.-S.; Seo, S.-W.; Cho, S. M.; Park, N.-G. Formamidinium and cesium hybridization for photo- and moisture-stable perovskite solar cell. *Adv. Energy Mater.* **2015**, *5*, 1501310.

(19) Binek, A.; Hanusch, F. C.; Docampo, P.; Bein, T. Stabilization of the trigonal high-temperature phase of formamidinium lead iodide. *J. Phys. Chem. Lett.* **2015**, *6*, 1249−1253.

(20) Niu, G.; Li, W.; Meng, F.; Wang, L.; Dong, H.; Qiu, Y. Study on the stability of $CH_3NH_3PbI_3$ films and the effect of post-modification by aluminum oxide in all-solid-state hybrid solar cells. *J. Mater. Chem. A* **2014**, *2*, 705−710.

(21) Williamson, G. K.; Hall, W. H. X-ray line broadening from filed aluminium and wolfram. *Acta Metall.* **1953**, *1*, 22−31.

(22) Zhao, Y.; Zhang, J. Microstrain and grain-size analysis from diffraction peak width and graphical derivation of high-pressure thermomechanics. *J. Appl. Crystallogr.* **2008**, *41*, 1095−1108.

(23) Sanchez-Bajo, F.; Cumbrera, F. L. The use of the pseudo-voigt function in the variance method of x-ray line-broadening analysis. *J. Appl. Crystallogr.* **1997**, *30*, 550−550.

(24) Kieslich, G.; Sun, S.; Cheetham, A. K. Solid-state principles applied to organic-inorganic perovskites: New tricks for an old dog. *Chem. Science* **2014**, *5*, 4712−4715.

(25) Sondena, R.; Stolen, S.; Ravindran, P.; Grande, T. Heat capacity and lattice dynamics of cubic and hexagonal $SrMnO_3$: Calorimetry and density functional theory simulations. *Phys. Rev. B: Condens. Matter Mater. Phys.* **2007**, *75*, 214307.

(26) Pascoe, A. R.; Yang, M.; Kopidakis, N.; Zhu, K.; Reese, M. O.; Rumbles, G.; Fekete, M.; Duffy, N. W.; Cheng, Y.-B. Planar versus mesoscopic perovskite microstructures: The influence of $CH_3NH_3PbI_3$ morphology on charge transport and recombination dynamics. *Nano Energy* **2016**, *22*, 439−452.

(27) Jeon, N. J.; Noh, J. H.; Kim, Y. C.; Yang, W. S.; Ryu, S.; Seok, S. I. Solvent engineering for high-performance inorganic−organic hybrid perovskite solar cells. *Nat. Mater.* **2014**, *13*, 897−903.

(28) Zheng, X.; Chen, B.; Wu, C.; Priya, S. Room temperature fabrication of $CH_3NH_3PbBr_3$ by anti-solvent assisted crystallization approach for perovskite solar cells with fast response and small J−V hysteresis. *Nano Energy* **2015**, *17*, 269−278.

(29) Nguyen, W. H.; Bailie, C. D.; Unger, E. L.; McGehee, M. D. Enhancing the hole-conductivity of spiro-OMeTAD without oxygen or lithium salts by using $spiro(TFSI)_2$ in perovskite and dye-sensitized solar cells. *J. Am. Chem. Soc.* **2014**, *136*, 10996−11001.